RSC Advances

PAPER

View Article Online
View Journal | View Issue

Cite this: *RSC Adv.*, 2021, **11**, 33179

Ultradispersed Ir_xNi clusters as bifunctional electrocatalysts for high-efficiency water splitting in acid electrolytes†

Xiaojie Zhao, Ying Chang,* Jiang Ji, Jingchun Jia* and Meilin Jia

Received 13th August 2021
Accepted 28th September 2021

DOI: 10.1039/d1ra06136d

rsc.li/rsc-advances

Design and synthesis of electrocatalysts with high activity and low cost is an important challenge for water splitting. We report a rapid and facile synthetic route to obtain Ir_xNi clusters *via* polyol reduction. The Ir_xNi clusters show excellent activity for the oxygen evolution reaction (OER) and hydrogen evolution reaction (HER) in acidic electrolytes. The optimized Ir_2Ni/C clusters exhibit an electrochemical active area of 18.27 mF cm^{-2}, with the overpotential of OER being 292 mV and HER being 30 mV at 10 mA cm^{-2}, respectively. In addition, the Ir_2Ni/C used as the cathode and anode for the H-type hydrolysis tank only needs 1.597 V cell voltages. The excellent electrocatalytic performance is mainly attributed to the synergistic effect between the metals and the ultra-fine particle size. This study provides a novel strategy that has a broad application for water splitting.

1. Introduction

Hydrogen energy as a clean energy has become a research hotspot in recent years. Electrolytic water[1,2] and fuel cells[3,4] are important devices for hydrogen energy generation and conversion.[5,6] These new technologies have been deemed to be clean, environmentally friendly and renewable, and they play extremely important roles in hydrogen energy technology. The use of these technologies is a promising strategy for the production of clean energy by electrocatalytic water splitting,[7] which involves the cathode HER[8–10] and the anode OER.[11–14] The product of electrolyzed water can be used as raw material for fuel cells. However, the OER is usually a complex electron transfer process with multistep coupling, which often shows hysteresis reaction kinetics,[15] thereby substantially affecting the reaction efficiency of water electrolysis.[16]

Pt,[17] Ru,[18] Pd[19] and other precious metal catalysts are used in both electrolytic water and fuel cells. However, owing to their expense and poor durability, large-scale commercial development is difficult. We attempt to introduce other elements and reduce particle size to enhance catalytic activity while reducing the amount of precious metals. Bimetallic electrocatalysts usually combine precious metals with transition metals, such as IrCu.[20,21] Ir-based[22–24] catalysts have higher activity and stability in alkaline electrolytes, but it is difficult to realize under acidic conditions because they easily dissolve and agglomerate. To overcome these barriers, it is necessary to design efficient and stable electrocatalysts in acidic media. The synergistic effect that is introduced by alloying reduces the adsorption energy of intermediates and further improves the catalytic performance.

Recently, the unique electronic structures and high surface atomic ratios have made metal clusters a new type of catalysts.[25,26] Researchers have successfully prepared Pt and Ru clusters of smaller particle size for OER. Moreover, these structures[27–30] can stabilize the metal clusters[31,32] during the removal of ligands. However, in conventional synthesis methods, clusters tend to agglomerate, which reduces their catalytic performance. Recent studies have shown that carbon supports[33,34] can overcome this obstacle by regulating charge transfer pathways and pores. Since the particle sizes of metal clusters are very small, more active sites can be exposed;[35] thus, our research group conducted relevant studies on them.

This study report that the synthesis of an Ir_xNi cluster catalyst in which a simple oil bath was used to control the element composition ratio by adjusting the proportion of the metal precursor, thereby avoiding complex processes, such as high-temperature annealing, and time-consuming steps.[36–38] The synthesized Ir_xNi clusters were distributed on a thin layer of carbon (Ir_xNi/C). Due to differences in atom sizes, the metals forms clusters by bonding; thus, the ultra-fine particle size (2 nm) can increase active sites. Based on the rapid synthetic applications of this work; it can be extended to other Ir-based clusters materials.

2. Experimental section

2.1 Experimental materials

Trisodium citrate dehydrate ($C_6H_5Na_3O_7 \cdot 2H_2O$, ≥99.0%), iridium(III) chloride hydrate ($IrCl_3 \cdot xH_2O$, 99.9%, Ir: 60%),

College of Chemistry and Environmental Science, Inner Mongolia Key Laboratory of Green Catalysis and Inner Mongolia Collaborative Innovation Center for Water Environment Safety, Inner Mongolia Normal University, Hohhot, 010022, China. E-mail: changying@imnu.edu.cn; jjc1983@126.com

† Electronic supplementary information (ESI) available. See DOI: 10.1039/d1ra06136d

nickel(II) chloride hexahydrate ($NiCl_2 \cdot 6H_2O$, ≥98.0%), Vulcan XC-72R carbon black, ethylene glycol ($C_2H_6O_2$, 99%), and potassium hydroxide (KOH, ≥85.0%) and Nafion solution (~5 wt%) were all purchased from Aladdin Industrial Corp. All the chemicals were used without further purification. The water (18.25 MΩ cm^{-1}) that was used in all experiments was prepared *via* passage through an ultrapure purification system (aqua solutions).

2.2 Materials synthesis

For the Ir_2Ni/C, 40 mg $C_6H_5Na_3O_7 \cdot 2H_2O$ was added into a round-bottomed flask of 30 mL ethylene glycol and ultrasonic dispersion to transparency. Then, 268 μL $NiCl_2 \cdot 6H_2O$ (0.2 g mL^{-1}) and 1445 μL $IrCl_3 \cdot xH_2O$ (0.1 g mL^{-1}) were added in to a flask, meanwhile add the magnetons and stir well. Then, 1 M KOH was added drop by drop to adjust pH to 9. Next, 40 mg XC-72R was added and dispersed evenly using ultrasound, and the oil bath is conducted under set conditions (160 °C, 300 rpm). The resulting mixture was washed *via* ethanol/ultrapure water and dried under vacuum. The preparations of IrNi/C, Ir_3Ni/C and Ir/C were similar to the preparation of Ir_2Ni/C except that 723 μL, 2168 μL, and 1667 μL $IrCl_3 \cdot xH_2O$ (0.1 g mL^{-1}) were used for IrNi/C, Ir_3Ni/C and Ir/C, respectively.

2.3 Materials characterization

Transmission electron microscopy (TEM) and High-resolution TEM (HRTEM, FEI Tecnai G2 F30) were conducted to morphology and structure. X-ray photoelectron spectroscopy (XPS, ESCALAB 250Xi) and X-ray diffraction (XRD, Rigaku Ultima IV) were conducted to chemical state and structure, the scan speed was set as 4° min^{-1} with 2θ range of 5–90°.

2.4 Electrochemical measurements

The electrochemical workstation was CHI 660E (Chenhua, Shanghai, China), and all tests were performed in three-electrode electrolytic tank. The working electrode was carbon paper (area: 0.25 cm^2), reference electrode (Ag/AgCl) and counter electrode (graphite rod) were used. The mixing Nafion (5%), ultrapure water and ethanol (1 : 9 : 10) into slurry to prepared working electrode. Then, 5 mg catalyst was weighed and dissolved in 1 mL prepared slurry to obtain a uniform dispersion. A total of 16 μL catalyst ink was measured and spread evenly on square carbon paper (loading amount: 0.32 mg cm^{-2}). The linear sweep voltammetry (LSV) were measured at a sweep rate of 5 mV s^{-1}. The C_{dl} was in the test range between potentials of 1–1.1 V with various sweep rates (10–100 mV s^{-1}). Electrochemical impedance spectroscopy (EIS)

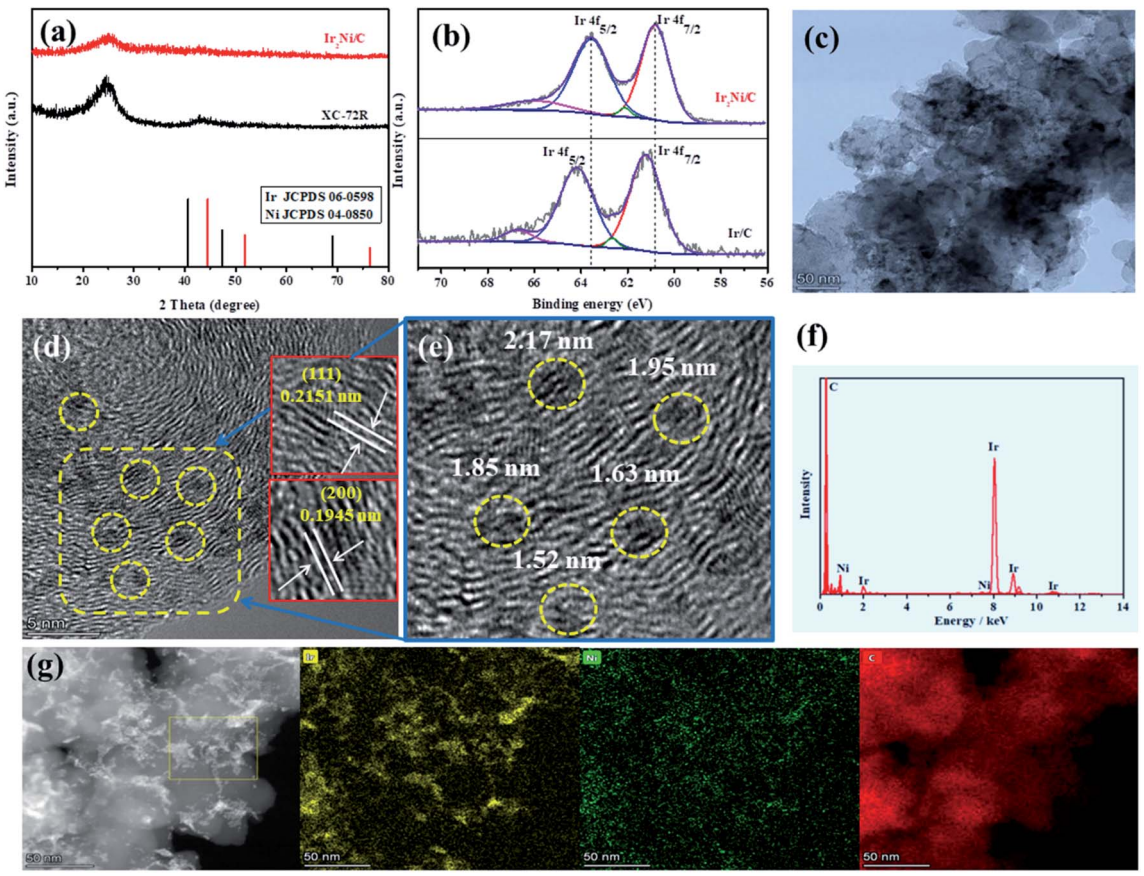

Fig. 1 (a) XRD patterns of Ir_2Ni/C, XC-72R Vulcan carbon. (b) XPS spectra of Ir_2Ni/C and Ir/C. (c) TEM image and (d) HRTEM image of Ir_2Ni/C. (e) Magnified HRTEM image that was recorded from the region that is marked in (d). (f) EDS spectrum. (g) HAADF-STEM image, Ir STEM-EDS mappings, Ni STEM-EDS mappings, and C STEM-EDS mappings that were obtained for Ir_2Ni/C.

of the OER was performed a test potential of 1.4 V and a frequency range (100–0.01 Hz). The chronopotentiometry parameter (CP) test was conducted at 10 mA cm^{-2}.

3. Results and discussion

The Ir_xNi/C (x = 1, 2, 3) clusters were prepared by polyol reduction (Fig. S1†). The composition ratio of Ir_xNi/C was determined by adjusting the mole ratio of the precursor (see Experimental section for details). X-ray diffraction (XRD) (Fig. 1a) pattern resemble that of the amorphous carbon support, only two broad diffraction peaks at 24.5° and 44.5° were readily observed, and there was no evidence of metal or metal oxide formation. In addition, with increasing Ni content, the peak strength of the clusters gradually decreased, and the half-peak width gradually increased (Fig. S2†), which indicate that the clusters were of low crystallinity and ultrafine sizes.[8,20,21] Moreover, compared with pure XC-72R, the peak strength decreased significantly; hence, the clusters were successfully loaded onto the carbon support. The change in peak strength also further demonstrates the occurrence of a synergistic effect in the cluster phase, which may have been caused by the replacement of Ni by Ir.

X-ray photoelectron spectroscopy (XPS) (Fig. S3†) was used to further investigate the changes in the electronic structure of the Ir_2Ni/C clusters. The Ir 4f spectrum shows that iridium was present mainly in the valence states of Ir^0 and Ir^{4+}, and the peaks at 61.1, 62.5, 64.0 and 66.5 eV correspond to Ir^0 $4f_{7/2}$, Ir^{4+} $4f_{7/2}$, Ir^0 $4f_{5/2}$, and Ir^{4+} $4f_{5/2}$, respectively; which indicating the surface of Ir_2Ni/C is mainly composed of Ir^0 (Fig. S3b†). As shown in Fig. S3c,† due to the low Ni content and insufficient signal-to-noise ratio, there are disorderly peaks in Ni 2p. In addition, the small peak of O 1s in the spectrum may have been partially oxidized exposure to air, and C was involved in a single bond and a double bond according to Fig. S3d.† Moreover, the Ir 4f peaks of Ir/C show a positive shift as presented in Fig. S4.† Fig. 1b shows that the Ir 4f peaks of Ir_2Ni/C clusters were significantly negatively shifted compared with Ir/C. The results demonstrate that Ir and Ni underwent electron transfer due to strong electron interactions.

The preparation of Ir_2Ni/C was monitored *via* transmission electron microscopy (TEM) (Fig. 1c). The results demonstrated that the clusters were uniformly distributed on the carbon support. Fig. 1d shows high-resolution TEM (HRTEM) image of Ir_2Ni/C, in which clusters are circled in yellow, and irregular clusters and defective surfaces can expose more active sites. The HRTEM image shows a continuous lattice fringe, which indicates the crystalline properties of the clusters, and the lattice fringe spacings were 0.2151 nm and 0.1945 nm,[21] which correspond to the (111) crystal plane and (200) crystal plane, respectively, of the face-centered cubic (fcc) Ir–Ni clusters (the inset of Fig. 1d). Therefore, the previous hypothesis of an amorphous phase was rejected, which may be because a low metal content leads to poor crystallinity. In combination with the previous XRD and XPS diagrams, the formation of Ir_2Ni/C clusters was further demonstrated, and the previous hypothesis of an amorphous phase was also rejected; due to the low metal content, there was no readily observable diffraction peak. Fig. 1e clearly shows the size of the clusters, which have a particle size of nearly 2 nm; therefore, clusters structure has been successfully formed. The electron diffraction spectrum (EDS) (Fig. 1f) shows that the distinct Ir, Ni and C peaks (from

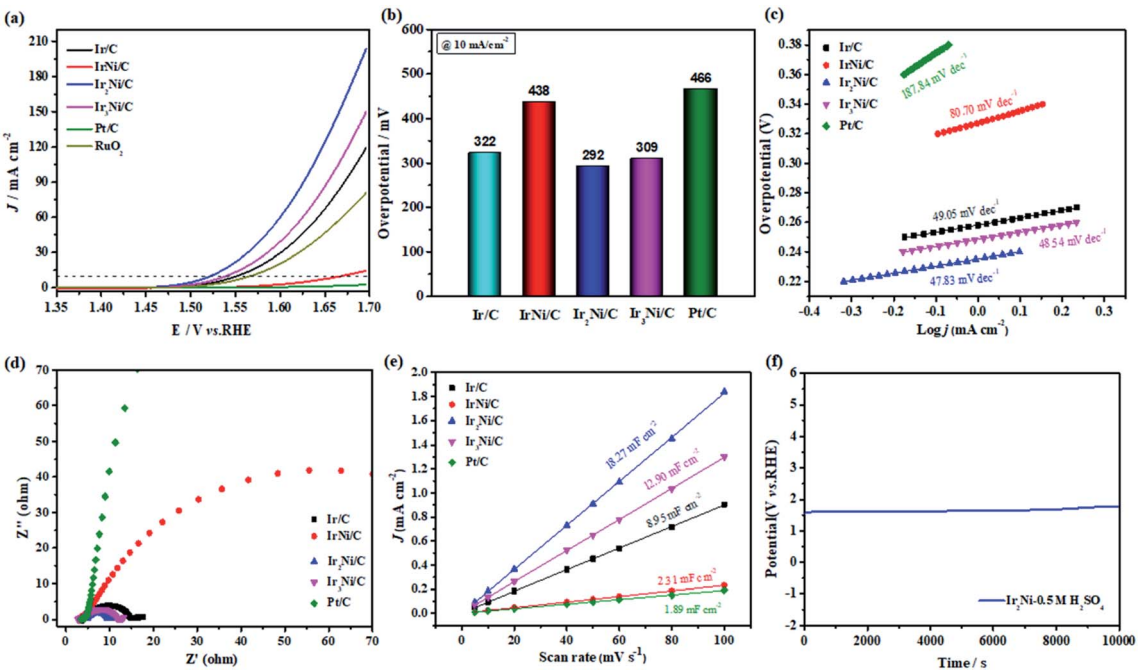

Fig. 2 (a) LSV curves of the OER in 0.5 M H_2SO_4. (b) The overpotential at 10 mA cm^{-2}. (c) Tafel slopes. (d) EIS results of the catalysts. (e) Electrical double layer capacitor (C_{dl}). (f) Chronopotentiometry curves of Ir_2Ni/C.

the yellow area in Fig. 1g) support the presence of Ir, Ni, and C. The Ir_2Ni/C clusters were characterized by high-angle circular dark field scanning (HAADF-STEM) (Fig. 1g), and the white particles in the figure clearly indicate the presence of metals. In addition, clusters are uniformly distributed without growth. The element mappings of Ir_2Ni/C showed that Ir, Ni and C are evenly distributed among the clusters, which further demonstrates the presence of iridium and nickel in the clusters. Compared to IrNi/C (Fig. S5†) and Ir_3Ni/C (Fig. S6†), Ir_2Ni/C is more uniformly distributed and has a smaller particle size than IrNi/C (4.3 nm) and Ir_3Ni/C (2.3 nm) (Fig. S7†).

Ir-based catalysts are considered excellent materials for OER in alkaline media.[24,39] However, their development in acidic media has been hindered by slow reaction kinetics, strong corrosion, and easy dissolution. Therefore, it is necessary to identify a catalyst that can overcome the acid barrier. Apart from that the Ir/C and Pt/C were used as the comparison samples of OER and HER, respectively. Fig. 2a exhibits the polarization curves of the OER. The Ir_2Ni/C clusters only require overpotential of 292 mV at 10 mA cm^{-2}, which is less than Ir/C (30 mV) and RuO_2 (48 mV) (Fig. 2b and Fig. S8†); hence, it has higher activity. Table S2† summarizes the performance of Ir-based catalysts of OERs in recent years. Moreover, by adding a suitable amount of nickel, the polarization curve is negatively shifted to a low potential, thereby reducing the reaction overpotential, which is mainly caused by the synergistic interaction between Ir and Ni species. Table S1† presents the metal content in Ir_xNi/C determined *via* inductively coupled plasma emission spectrometry (ICP-OES), with commercial contrast catalyst as references. The results show that low noble metal loading can still show excellent catalytic activity. In order to gain further insight into the catalytic ability and structural changes of OER, we performed XPS (Fig. S9†) characterization of Ir_2Ni/C after OER. It can be clearly seen in Fig. S9† that the binding energy of the Ir 4f peak becomes higher during the OER process, indicating the surface oxidation of Ir. These results suggest that Ir_2Ni/C forms IrO_x species on the catalyst surface during the OER process.[40,41]

In addition, compared to IrNi/C and Ir_3Ni/C (Fig. S5 and S6†), the enhancement of Ir_2Ni/C activity is also due to its uniform dispersion and ultrafine particle size (Fig. S7†). The Tafel slopes (Fig. 2c) of Ir_2Ni/C, Ir_3Ni/C, Ir/C, Pt/C and IrNi/C are 47.83, 48.54, 49.05, 80.70 and 187.84 mV dec^{-1}, respectively. The smaller Ir_2Ni/C indicated the low overpotential that is required in the reaction, which accelerated the kinetics. To further investigate the OER kinetic performance, the electrochemical impedance was tested. Charge transfer resistance (R_{ct}) occurred due to the strong interactions between atoms in the electrocatalytic process, and a smaller semicircle diameter indicated faster charge transfer and better catalytic performance (Fig. 2d). Furthermore, in the hydrogen adsorption/desorption zone;[42] the electrochemical double-layer capacitances (C_{dl}), which are linearly related to the electrochemical surface areas (ECSAs) were measured *via* cyclic voltammetry to evaluate the catalytic activity. The capacitance can be indirectly characterized by measuring the CV at various sweeping speeds (Fig. S10†). The C_{dl} (Fig. 2e) of Ir_2Ni/C is as high as 18.27 mF cm^{-2}, which represents a 2-fold improvement in C_{dl} over that of Ir/C. Ir_2Ni/C shows significantly enhanced ECSA compared with Ir/C, which further demonstrated that the appropriate amount of Ni exposed more active sites. In the chronopotentiometry test (Fig. 2f), the Ir_2Ni/C demonstrated excellent stability for 10 000 s

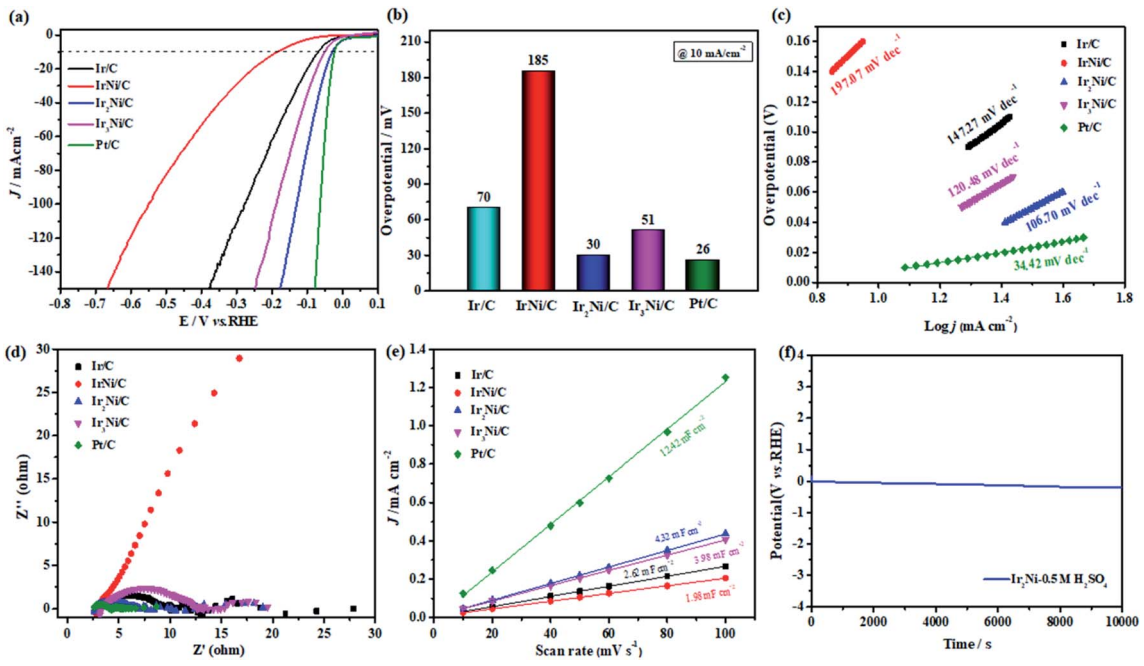

Fig. 3 (a) LSV curves of the HER in 0.5 M H_2SO_4. (b) The overpotential at 10 mA cm^{-2}. (c) Tafel slopes. (d) EIS results of the catalysts. (e) Electrical double layer capacitor (C_{dl}). (f) Chronopotentiometry curves of Ir_2Ni/C.

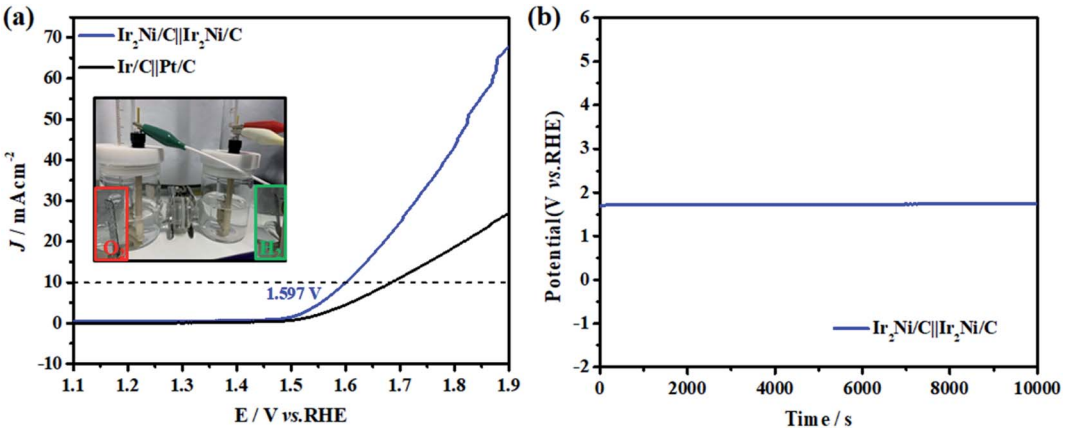

Fig. 4 (a) The polarization curves of $Ir_2Ni/C||Ir_2Ni/C$ and Ir/C||Pt/C toward overall water splitting. (b) The chronopotentiometric curve of $Ir_2Ni/C||Ir_2Ni/C$ for overall water splitting at a constant current density of 10 mA cm^{-2}.

(10 mA cm^{-2}) in acidic media. Then, we compared the polarization curves of Ir_2Ni/C before and after durability to reflect its activity reproducibility (Fig. S11†). After 10 000 s durability test, its activity decreased by only 25 mV at the 10 mA cm^{-2}. In addition, the current density represents a 2.4-fold improvement in the polarization curve (Fig. S12a†), a 3.4-fold improvement in C_{dl} (Fig. S12d†), and lower Tafel slopes (Fig. S12b†) and EIS (Fig. S12c†) in alkaline medium. The results show that the Ir_xNi clusters are more suitable for acidic medium.

The prepared catalyst was evaluated for HER in the same medium. Pt/C is considered the best catalyst for the HER,[43] especially because its overpotential tends to zero and its Tafel slope is much lower in acidic solutions. Iridium, which is an independent metal under typical conditions, is often insensitive to HER, but the formation of clusters of Ir_xNi/C can significantly improve its catalytic performance.[44] Fig. 3a shows the LSV curves of HER in acidic medium. Ir_2Ni/C provided higher activity (only a 30 mV overpotential) (Fig. 3b) and low Tafel slope (106.70 mV dec^{-1}) (Fig. 3c). Table S3† describes in detail the Ir-based catalysts that have been used in HER in recent years. Moreover, in the electrochemical impedance spectroscopy (EIS) test (Fig. 3d), the small R_{ct} indicates that it has superior charge transfer capability and kinetics.[45] Although the double electric layer capacitance (Fig. 3e) of Ir_2Ni/C, which is less than Pt/C, it represents 1.6-fold improvement over the C_{dl} of Ir/C. Soon afterwards, the same test was conducted in an alkaline medium. Due to differences in the HER paths and the influence of high pH, the HER activity in alkaline media is slightly inferior. Although a high current density (Fig. S13a†) could be realized, the initial potential and Tafel slope value (Fig. S13b†) were large due to the large background current. Compared with the acidic conditions, the double electric layer capacitance (C_{dl}) showed a downward trend (Fig. S13d†). However, the electrochemical impedance (Fig. S13c†) of Ir_2Ni/C is better than commercial Pt/C, which may be acceleration of the reaction kinetics by the electron synergy between Ir and Ni atoms. Ir_2Ni/C also demonstrates excellent stability. As shown in Fig. 3f, we further assess the long-term stability of Ir_2Ni/C. Ir_2Ni/C is stable up to 10 000 s (10 mA cm^{-2}) with no significant potential change to be negligible, thus, Ir_2Ni/C is stable for HER in highly corrosive acidic solution. This is due to the rough surfaces of the clusters and the reduction of the metal Ni–Ni bond length and the chemical reaction activation energy after alloying, which further improves the long-term stability of catalysts.

Considering that the self-supported[46] Ir_2Ni/C material has excellent bifunctional properties, we used Ir_2Ni/C as cathode and anode, respectively, to fabricate an electrolyzer ($Ir_2Ni/C||Ir_2Ni/C$) toward overall water splitting (the inset of Fig. 4a), which used as cathode and anode for H-type hydrolysis tank only needs 1.597 V cell voltages well below Ir/C||Pt/C (1.690 V) and other reported articles (Fig. 4a). In addition, the electrolyzer is durable up to 10 000 s (Fig. 4b).[47] The Faradaic efficiency (FE) of $Ir_2Ni/C||$ Ir_2Ni/C was experimentally measured to be 99%, and the gas production ($H_2 : O_2$) being close to 2 : 1 tested by drainage method (Fig. S14†). The Ir_2Ni/C is an outstanding bifunctional catalyst for overall water splitting.

Compared to the previously reported Ir-based materials (Tables S2 and S3†), Ir_2Ni/C has excellent catalytic properties for OER and HER, which main reasons can be summarized as follows: (1) the strong electron interaction between the precious metal Ir and the 3d transition metal Ni promotes electron transfer and accelerates the reaction kinetics. (2) Cluster structures are formed with nanometer particle sizes of nearly 2 nm, which can increase the ECSAs and further improve the catalytic performance. (3) Carbon support not only increases the electrical conductivity, but also inhibits the agglomeration of metal clusters into larger particles.

4. Conclusions

In summary, Ir_xNi/C cluster catalysts were synthesized *via* simple method. Ir_xNi/C clusters with average particle sizes of less than 2 nm were successfully prepared, and the abundant active sites and rough surface enhance the catalytic activity. The synthesized Ir_2Ni/C performs excellent bifunctional catalyst, the Ir_2Ni/C used as cathode and anode for H-type hydrolysis tank only needs 1.597 V cell voltages with long-term stability. This study provides valuable information and a novel strategy for

relevant industrial production by preparing Ir_2Ni/C bifunctional catalysts, so this strategy has broad application prospects in water splitting.

Conflicts of interest

No competing economic interests are declared by the authors.

Acknowledgements

We would like to thank the National Natural Science Foundation of China (Project No. 21703249), the Natural Science Foundation of Inner Mongolia of China (2019MS2017), the Research Innovation Foundation for Graduate of Inner Mongolia Normal University (No. CXJJS20105), the Research Innovation Foundation for Graduate of Inner Mongolia Autonomous Region (No. SZ2020116) and the Research Foundation for Advanced Talents of Inner Mongolia Normal University (No. 2018YJRC001 and 2018YJRC012) for financial support.

References

1 Q. Wang, C. Q. Xu, W. Liu, S. F. Hung, H. Bin Yang, J. Gao, W. Cai, H. M. Chen, J. Li and B. Liu, *Nat. Commun.*, 2020, **11**, 4246–4258.
2 H. N. Nong, T. Reier, H.-S. Oh, M. Gliech, P. Paciok, T. H. T. Vu, D. Teschner, M. Heggen, V. Petkov, R. Schlögl, T. Jones and P. Strasser, *Nat. Catal.*, 2018, **1**, 841–851.
3 Y. Li, Z. Kang, J. Mo, G. Yang, S. Yu, D. A. Talley, B. Han and F.-Y. Zhang, *Int. J. Hydrogen Energy*, 2018, **43**, 11223–11233.
4 O. Panchenko, E. Borgardt, W. Zwaygardt, F. J. Hackemüller, M. Bram, N. Kardjilov, T. Arlt, I. Manke, M. Müller, D. Stolten and W. Lehnert, *J. Power Sources*, 2018, **390**, 108–115.
5 X. Shi, H. Wang, P. Kannan, J. Ding, S. Ji, F. Liu, H. Gai and R. Wang, *J. Mater. Chem. A*, 2019, **7**, 3344–3352.
6 L. Rößner and M. Armbrüster, *ACS Catal.*, 2019, **9**, 2018–2062.
7 J. Feng, F. Lv, W. Zhang, P. Li, K. Wang, C. Yang, B. Wang, Y. Yang, J. Zhou, F. Lin, G.-C. Wang and S. Guo, *Adv. Mater.*, 2017, **29**, 1703798.
8 Q. Wang, M. Ming, S. Niu, Y. Zhang, G. Fan and J.-S. Hu, *Adv. Energy Mater.*, 2018, **8**, 1801698.
9 S. Li, P. Ren, C. Yang, X. Liu, Z. Yin, W. Li, H. Yang, J. Li, X. Wang, Y. Wang, R. Cao, L. Lin, S. Yao, X. Wen and D. Ma, *Sci. Bull.*, 2018, **63**, 1358–1363.
10 S. Li, R. Cao, M. Xu, Y. Deng, L. Lin, S. Yao, X. Liang, M. Peng, Z. Gao and Y. Ge, *Natl. Sci. Rev.*, 2021, DOI: 10.1093/nsr/nwab026.
11 Y. Liu, Y. Ying, L. Fei, Y. Liu, Q. Hu, G. Zhang, S. Y. Pang, W. Lu, C. L. Mak, X. Luo, L. Zhou, M. Wei and H. Huang, *J. Am. Chem. Soc.*, 2019, **141**, 8136–8145.
12 J. Hu, S. Li, J. Chu, S. Niu, J. Wang, Y. Du, Z. Li, X. Han and P. Xu, *ACS Catal.*, 2019, **9**, 10705–10711.
13 Y. Li, Z. Wang, J. Hu, S. Li, Y. Du, X. Han and P. Xu, *Adv. Funct. Mater.*, 2020, **30**, 1910498.
14 S. Niu, X.-P. Kong, S. Li, Y. Zhang, J. Wu, W. Zhao and P. Xu, *Appl. Catal., B*, 2021, **297**, 120440.
15 O. Matselko, R. R. Zimmermann, A. Ormeci, U. Burkhardt, R. Gladyshevskii, Y. Grin and M. Armbrüster, *J. Phys. Chem. C*, 2018, **122**, 21891–21896.
16 Q. Jiang, J. Xu, Z. Li, C. Zhou, X. Chen, H. Meng, Y. Han, X. Shi, C. Zhan, Y. Zhang, Q. Zhang, X. Jia and R. Zhang, *Adv. Mater. Interfaces*, 2021, **20**, 2002034.
17 J. Liu, M. Jiao, B. Mei, Y. Tong, Y. Li, M. Ruan, P. Song, G. Sun, L. Jiang, Y. Wang, Z. Jiang, L. Gu, Z. Zhou and W. Xu, *Angew. Chem., Int. Ed.*, 2019, **58**, 1163–1167.
18 J. Xu, J. Li, Z. Lian, A. Araujo, Y. Li, B. Wei, Z. Yu, O. Bondarchuk, I. Amorim, V. Tileli, B. Li and L. Liu, *ACS Catal.*, 2021, **11**, 3402–3413.
19 J. Zhu, M. Xie, Z. Chen, Z. Lyu, M. Chi, W. Jin and Y. Xia, *Adv. Energy Mater.*, 2020, **10**, 1904114.
20 F. Wang, K. Kusada, D. Wu, T. Yamamoto, T. Toriyama, S. Matsumura, Y. Nanba, M. Koyama and H. Kitagawa, *Angew. Chem., Int. Ed.*, 2018, **57**, 4505–4509.
21 Y. Pi, J. Guo, Q. Shao and X. Huang, *Chem. Mater.*, 2018, **30**, 8571–8578.
22 X. Shi, H. Zhu, J. Du, L. Cao, X. Wang and H.-P. Liang, *Electrochim. Acta*, 2021, **370**, 137710.
23 J. Shan, C. Ye, S. Chen, T. Sun, Y. Jiao, L. Liu, C. Zhu, L. Song, Y. Han, M. Jaroniec, Y. Zhu, Y. Zheng and S. Z. Qiao, *J. Am. Chem. Soc.*, 2021, **143**, 5201–5211.
24 S. M. Alia, S. Shulda, C. Ngo, S. Pylypenko and B. S. Pivovar, *ACS Catal.*, 2018, **8**, 2111–2120.
25 P. Li, Z. Jin, Y. Qian, Z. Fang, D. Xiao and G. Yu, *ACS Energy Lett.*, 2019, **4**, 1793–1802.
26 L. Liu and A. Corma, *Chem. Rev.*, 2018, **118**, 4981–5079.
27 P. Li, Z. Jin, Z. Fang and G. Yu, *Angew. Chem., Int. Ed.*, 2020, **59**, 22610–22616.
28 J. Li, G. Zhan, J. Yang, F. Quan, C. Mao, Y. Liu, B. Wang, F. Lei, L. Li, A. W. M. Chan, L. Xu, Y. Shi, Y. Du, W. Hao, P. K. Wong, J. Wang, S. X. Dou, L. Zhang and J. C. Yu, *J. Am. Chem. Soc.*, 2020, **142**, 7036–7046.
29 J. Zhang, H. Zhang and Y. Huang, *Appl. Catal., B*, 2021, **297**, 120453.
30 S. L. Zhang, X. F. Lu, Z. P. Wu, D. Luan and X. W. D. Lou, *Angew. Chem., Int. Ed.*, 2021, **60**, 19068–19073.
31 Z. Jin and A. J. Bard, *Proc. Natl. Acad. Sci. U. S. A.*, 2020, **117**, 12651–12656.
32 J. Zhang, F. Xing, H. Zhang and Y. Huang, *Dalton Trans.*, 2020, **49**, 13962–13969.
33 M. Liu, F. Hof, M. Moro, G. Valenti, F. Paolucci and A. Penicaud, *Nanoscale*, 2020, **12**, 20165–20170.
34 Y. Huang, S. L. Zhang, X. F. Lu, Z. P. Wu, D. Luan and X. W. D. Lou, *Angew. Chem., Int. Ed.*, 2021, **60**, 11841–11846.
35 P. Li, Z. Jin, Z. Fang and G. Yu, *Energy Environ. Sci.*, 2021, **14**, 3522–3531.
36 Z. Liu, J. Mao, T.-H. Liu, G. Chen and Z. Ren, *MRS Bull.*, 2018, **43**, 181–186.
37 L. Fu, G. Cheng and W. Luo, *J. Mater. Chem. A*, 2017, **5**, 24836–24841.
38 W. H. Lee, J. Yi, H. N. Nong, P. Strasser, K. H. Chae, B. K. Min, Y. J. Hwang and H. S. Oh, *Nanoscale*, 2020, **12**, 14903–14910.

39 P. Jiang, J. Chen, C. Wang, K. Yang, S. Gong, S. Liu, Z. Lin, M. Li, G. Xia, Y. Yang, J. Su and Q. Chen, *Adv. Mater.*, 2018, **30**, 1705324.
40 L. Fu, F. Yang, G. Cheng and W. Luo, *Nanoscale*, 2018, **10**, 1892–1897.
41 D. Weber, L. M. Schoop, D. Wurmbrand, S. Laha, F. Podjaski, V. Duppel, K. Müller, U. Starke and B. V. Lotsch, *J. Mater. Chem. A*, 2018, **6**, 21558–21566.
42 F. Li, G. F. Han, H. J. Noh, J. P. Jeon, I. Ahmad, S. Chen, C. Yang, Y. Bu, Z. Fu, Y. Lu and J. B. Baek, *Nat. Commun.*, 2019, **10**, 4060–4067.
43 J. N. Tiwari, S. Sultan, C. W. Myung, T. Yoon, N. Li, M. Ha, A. M. Harzandi, H. J. Park, D. Y. Kim, S. S. Chandrasekaran, W. G. Lee, V. Vij, H. Kang, T. J. Shin, H. S. Shin, G. Lee, Z. Lee and K. S. Kim, *Nat. Energy*, 2018, **3**, 773–782.
44 S. Liu, Z. Hu, Y. Wu, J. Zhang, Y. Zhang, B. Cui, C. Liu, S. Hu, N. Zhao, X. Han, A. Cao, Y. Chen, Y. Deng and W. Hu, *Adv. Mater.*, 2020, **3**, 2006034.
45 D. Wang, Q. Li, C. Han, Q. Lu, Z. Xing and X. Yang, *Nat. Commun.*, 2019, **10**, 3899–3911.
46 F. Godínez-Salomón, L. Albiter, S. M. Alia, B. S. Pivovar, L. E. Camacho-Forero, P. B. Balbuena, R. Mendoza-Cruz, M. J. Arellano-Jimenez and C. P. Rhodes, *ACS Catal.*, 2018, **8**, 10498–10520.
47 Y. Peng, Q. Liu, B. Lu, T. He, F. Nichols, X. Hu, T. Huang, G. Huang, L. Guzman, Y. Ping and S. Chen, *ACS Catal.*, 2021, **11**, 1179–1188.